



Kent Academic Repository

Sasikumar, Yadukrishnan, Nuttall, William.J. and Mason, Nigel (2024) *An experimental apparatus to study the adsorption of water on proxies for spent nuclear fuel surfaces.* Measurement Science and Technology, 35 (11). ISSN 0957-0233.

Downloaded from

<https://kar.kent.ac.uk/106868/> The University of Kent's Academic Repository KAR

The version of record is available from

<https://doi.org/10.1088/1361-6501/ad67fa>

This document version

Publisher pdf

DOI for this version

Licence for this version

CC BY (Attribution)

Additional information

Versions of research works

Versions of Record

If this version is the version of record, it is the same as the published version available on the publisher's web site. Cite as the published version.

Author Accepted Manuscripts

If this document is identified as the Author Accepted Manuscript it is the version after peer review but before type setting, copy editing or publisher branding. Cite as Surname, Initial. (Year) 'Title of article'. To be published in **Title of Journal**, Volume and issue numbers [peer-reviewed accepted version]. Available at: DOI or URL (Accessed: date).

Enquiries

If you have questions about this document contact ResearchSupport@kent.ac.uk. Please include the URL of the record in KAR. If you believe that your, or a third party's rights have been compromised through this document please see our [Take Down policy](https://www.kent.ac.uk/guides/kar-the-kent-academic-repository#policies) (available from <https://www.kent.ac.uk/guides/kar-the-kent-academic-repository#policies>).

An experimental apparatus to study the adsorption of water on proxies for spent nuclear fuel surfaces

Yadukrishnan Sasikumar^{1,3,*} , William J Nuttall¹  and Nigel J Mason² 

¹ School of Engineering and Innovation, The Open University, Milton Keynes, United Kingdom

² School of Physical Sciences, University of Kent, Canterbury, United Kingdom

E-mail: sasikumary@ornl.gov

Received 19 February 2024, revised 18 July 2024

Accepted for publication 25 July 2024

Published 13 August 2024



Abstract

This paper describes the design, construction and testing of an experimental apparatus capable of conducting high temperature adsorption isotherm analyses on large quantities of powder samples inside an ultra-high vacuum chamber. Data is obtained by dosing in fixed amounts of water vapor and measuring precise pressure changes using a high temperature capacitance manometer. The rig is designed to provide insight into the wetting of failed spent nuclear fuel (SNF) under conditions conventionally regarded as ‘dry’. Validation experiments are reported based on powder CeO₂ (a non-radioactive surrogate for SNF) at 100 °C. It is planned that this and successor rigs can provide ever more direct experimental evidence to address a key policy-relevant problem.

Keywords: spent nuclear fuel disposal, spent nuclear fuel management, water-fuel interaction, spent nuclear fuel drying

1. Introduction

The current nuclear waste management plan in most nuclear countries involves storing spent nuclear fuel (SNF) in cooling ponds before transferring it to dry casks after it stops generating significant decay heat. The dry casks are generally stored in cement overpacks pending final disposal in facilities such as a deep geological repository. Fuel failure from reactor operation is an issue that has been widely studied and the detectable damage ratio is close to 0.001%, i.e. ~14 leaks per million rods loaded for modern pressurized water

reactors [1]. The types of defects include pin-hole defects, cracks, and large breaks [2]. Depending on the extent of the breach in the cladding, the failed fuel can either be identified from pond radioactivity levels or in some cases, go into disposal unnoticed. Damaged SNF in storage presents a possibility that hot, radioactive fuel will come into contact with water. This leads to two important questions—‘Can thermally hot spent fuel attract/adsorb water at low pressures?’; and ‘Does failed fuel exposed to water/steam pose a safety hazard in the long term?’ These questions make it vital to understand the wetting of SNF in drying pressures and temperatures as the assumptions leading to repository safety cases might perhaps be too far from the reality. Wet failed fuel in storage is a less explored conundrum due to the various corrosion phases and their stabilities in repository environments [3]. The paper presents an experimental approach to explore such questions and probe the surface science of water adsorption on SNF surfaces at drying temperatures qualitatively and quantitatively.

³ Oak Ridge National Laboratory, Nuclear Energy and Fuel Cycle Division, Oak Ridge, Tennessee 37831.

* Author to whom any correspondence should be addressed.



Original content from this work may be used under the terms of the [Creative Commons Attribution 4.0 licence](https://creativecommons.org/licenses/by/4.0/). Any further distribution of this work must maintain attribution to the author(s) and the title of the work, journal citation and DOI.

Two trends seen in water adsorption over metal-oxide surfaces, like in SNFs, are molecular and dissociative adsorption of the water molecule based on surface energies. Molecular adsorption features the oxygen ion atop the surface cation with weak hydrogen bonding between the hydrogen ions of the water molecule and the surface oxygen ions. Dissociative adsorption involves the formation of two hydroxyl groups, after the hydrogen ion (from H_2O) dissociates to form a hydroxyl group with the surface oxygen ion. Studies exploring adsorption of water on metal-oxide surfaces propose a mechanism where initial monolayers are adsorbed by dissociative chemisorption based on surface defects, followed by multilayers of molecular physisorption [4]. Dissociative chemisorption of water on SNF surfaces can lead to a build-up of hydrogen partial pressures and is an area of interest with regards to long-term storage of SNF [5].

Stakebake and Steward reported a mass spectrometric thermal desorption study of water interactions with plutonium dioxide as an example of the adsorption characteristics of water on actinide dioxide surfaces at high temperatures [6]. The Stakebake and Steward study presents adsorption isotherm curves for water on PuO_2 at 30 °C, 50 °C and 85 °C showing adsorption in all conditions. The results from the current study have been compared against those from Stakebake and Steward in section 4. The studies show consistent results with respect to adsorption characteristics while looking at ceria and PuO_2 . Gravimetric studies of water–actinide dioxide interaction using Quartz crystal microbalance and an analytical balance have also been reported in the literature [7, 8]. Despite this earlier work, many details on how water molecules orient and adsorb on actinide dioxide surfaces at SNF drying temperatures (100 °C–200 °C) remain to be unravelled. These gaps in understanding can be attributed to a dearth in experimental results to validate model predictions. Furthermore, there is also a gap in the experimental results complementing computational hypotheses of surface energies and subsequent adsorption preferences on different principal surface atomic orientations and over lattice defects [4,9–11]. These are needed to understand those conditions that favour dissociative adsorption (hydroxylation) and the resulting effects such as H_2 build-up or water carryover.

Molecular physisorption can lead to the wetting and potential corrosion of the fuel matrix [12]. Looking at the radiochemical aspect of fuel–water interactions: when the fuel is exposed to water, there are multiple reactions that can take place based on the surface corrosion potential and accessible fuel inventory [13]. The accessible fuel inventory is associated with the fuel components in different regions (gaps, grain boundaries vs bulk) and their potential ease of diffusion [14]. Dissolution mechanisms for potential fuel surface corrosion are based on two competing reactions: A radiolysis driven dissolution, and a slower conventional chemical dissolution of the SNF matrix [13]. The radiolytic corrosion is a result of the radiolytic products, including ions (H_3O^+), electrons, radicals ($\cdot\text{OH}$), atoms (H^*), and molecular products (H_2O_2 , H_2), formed from the interaction of ionizing radiation of the

fuel on water [15]. These radiolytic products change the local redox conditions around the fuel facilitating fuel oxidation and subsequent dissolution [16,17]. Conventional chemical dissolution of the fuel prevails in the absence of the strong oxidizing radiolytic products, and the fuel continues to degrade until solution saturation is achieved or external influences such as H_2 or insoluble U(VI) secondary precipitates are formed. In the scenario discussed here, where failed fuel goes into storage with accumulated water, the precise mechanisms and rates at which fuels corrode over extended time scales are not fully understood. While knowing the risks arising from the chemical integrity of failed fuel after thousands of years is of vital importance, this would require a greater understanding of the presence and availability of water that could lead to such interactions.

This paper discusses an experimental apparatus that has been designed to investigate such fuel–water adsorption models. Characterization of the apparatus and validation of the experimental methodology was performed by conducting high temperature (100 ± 5 °C) water vapor adsorption isotherm experiments on CeO_2 , a surrogate for SNF surfaces. The data has been compared with similar studies from the literature on powder PuO_2 surfaces.

2. Design of the experimental apparatus

The experimental apparatus was designed to mimic SNF drying conditions at both high temperatures (up to 200 °C) and in low vacuum environments. The apparatus was also equipped to go to ultra-high vacuum pressures of 1.0×10^{-7} mbar for sample pre-treatment. The boundary conditions for maximum pressure were set at water bulk saturation pressures where adsorption is assumed to prevail.

Figure 1 shows the apparatus that was assembled for the study. A six-way cross formed the main experimental chamber with flanges extending to: (1) the pumping system; (2) the sample holder; (3) the gas line; (4) a combi pressure gauge; and (5) a burst disc for safety from accidental overpressures. A gate valve was added between the chamber and the turbopump in order to isolate the chamber during the experiments. This was essential since the experiment required to measure pressure equilibrations in the chamber as a function of dosing water vapour into it. Additionally, an L-extension was also added to the pumping line, after the gate valve, to prevent any spillage of sample into the turbo pump during pump down. To ensure that the adsorption is limited to the sample at a specific temperature, a separate sample holder heating unit was designed as shown in figure 2.

A gas line with an *in-situ* leak valve was used to dose fixed amounts of water vapor into the chamber and an MKS Baratron® Heated Dual—Range Absolute Capacitance Manometer (Model—D28D12TCEE0B0) was used to measure the pressure variations in the gas line prior to dosing, and the chamber as a result of water vapor adsorption on the

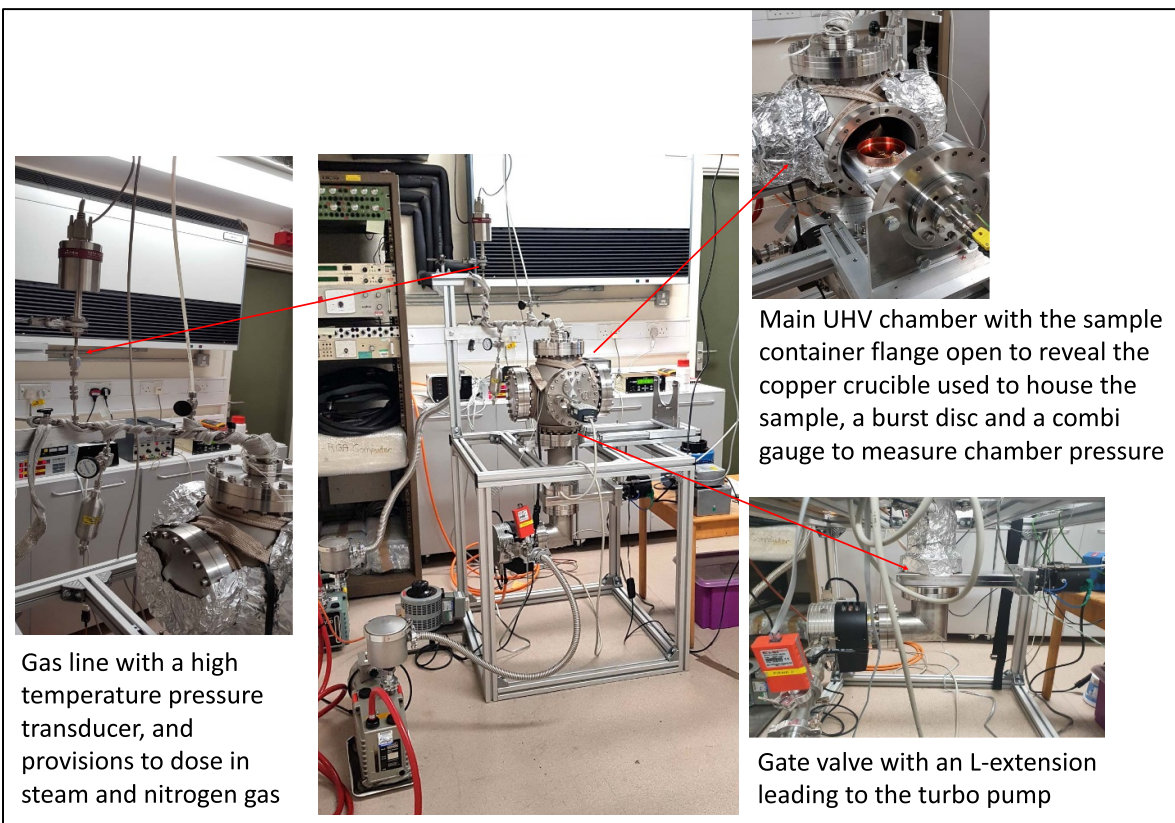


Figure 1. The SNF drying experimental apparatus with inserts showing the main components.

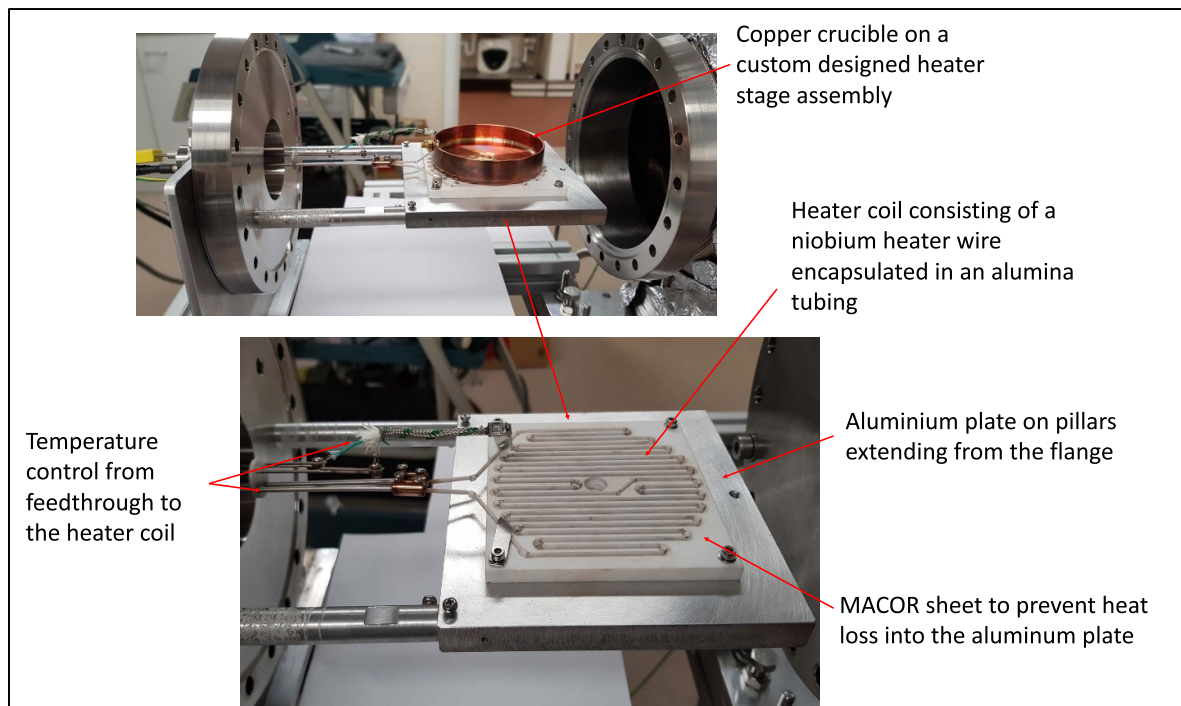


Figure 2. The sample holder flange highlighting the custom-made heater stage.

sample. A capacitance manometer was chosen for the experiment due to its superior accuracy of $\pm 0.25\%$ of reading with a resolution of 0.001% of the full-scale. A further advantage

is that the pressure measured by a Baratron is insensitive to the gas that it measures unlike Pirani and Ion gauges. The key attribute of this specific transducer model is its capability to

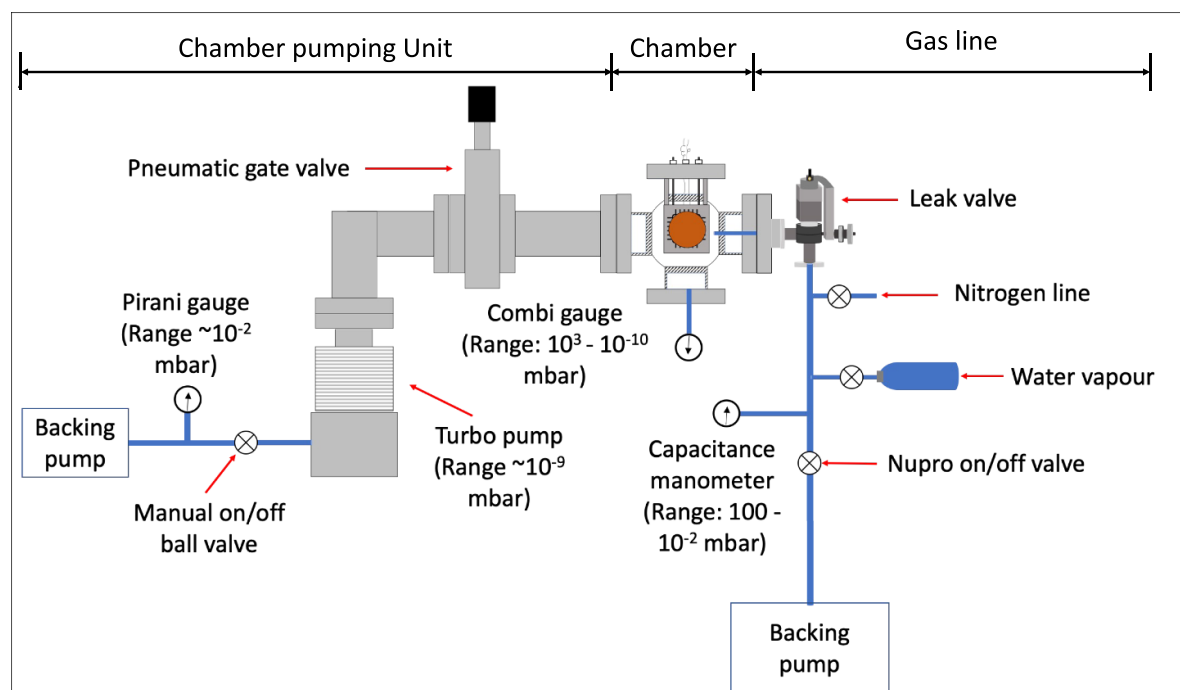


Figure 3. A schematic blueprint highlighting the different sections and bits of the experimental rig.

control the operating temperature at 100 °C. This allows the transducer to minimize the effects of temperature variations from the heating tapes surrounding the gas line and avoids any water vapour condensation on the pressure sensor surface.

The apparatus was designed for powder samples. A sample holder was designed to hold the powder sample allowing for enough sample mass with a vastly larger surface area of powder compared to inner surface area of the chamber. The sample holder was also required to be easily accessible for frequent sample changes and needed a provision to be able to be maintained in a specific equilibrium temperature throughout. This was made possible by heating the sample holder and the main chamber. Conductive heat losses through the flange pillars make it possible to maintain the sample holder at a lower temperature than the chamber walls at all times, and especially when the difference was small.

Figure 2 shows the sample holder flange design. It consists of a copper crucible, of 86 mm inner diameter \times 2.5 mm height \times 1.84 mm thickness. The crucible sits on a custom-made heating stage that was controlled using a Redlion PXU30020 proportional—integral—derivative (PID) controller. Figure 2 also shows the design and assembly of the heater setup along with the Nb—Al₂O₃ heater coil design that was used to make the heater. The coil was secured by precision boring the heater coil design into a MACOR[®] sheet and creating a recess in the sheet for the heater to be placed in, for good thermal contact. The temperature input for the PID was from a K-type thermocouple connected to the crucible through the flange feedthrough. The overall sample holder assembly was housed on an aluminium plate that was screwed onto extension pillars on the main chamber flange which enabled the sample

to slide into the middle of the chamber for the isotherm experiments. The frame extension slides (seen in figure 1) in either direction allowing additional support while opening or closing the flange/chamber for sample changes. Special nuts were placed to secure the flange from tipping on its weight.

The UHV chamber and gas line were also heated independently during the course of the experiment in order to maintain a higher thermal equilibrium than the sample and for avoiding any risk of bulk condensation of water in the gas line. This also meant that the water vapour would favour adsorption on the (colder) sample surface than the hotter chamber walls. As mentioned earlier, the sample temperature was PID controlled but the ambient rig temperature was not controlled by PID. Instead, separate heating tapes were used for the UHV chamber and the gas line and were controlled using variable transformers to maintain the temperature a few degrees above the sample temperature.

The approximate surface areas of the main chamber and the gas line were calculated as \sim 0.320 m² and 0.018 m² respectively. The crucible holder holds a volume of \sim 14.5 cc, allowing for a 10 gm micron sized powder sample to have at least 500 times the surface area of the chamber assuming loose packing and good gas access. Figure 3 is a schematic of the entire experiment apparatus. The chamber volume, in which the sample is placed, encompasses the volume between the gate valve and the leak valve as seen in figure 3. A gas line setup capable of dosing in fixed pressures of steam and other gases (as required) was built for the experiment and connected to the chamber through the manual leak valve. The gas line was designed to dose in water vapor and nitrogen for adsorption isotherm and volume estimations respectively. However,

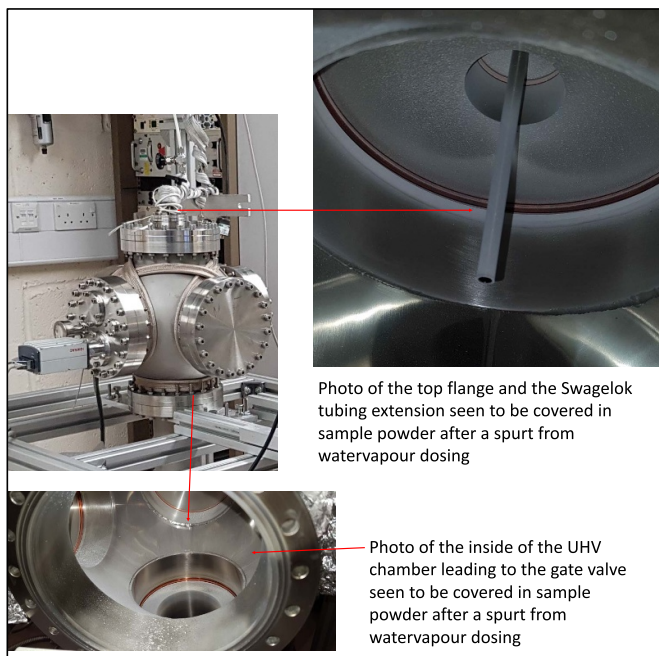


Figure 4. Images from inside the chamber showing the extent of powder spurted inside.

there is a provision to add other gases if required. A rotary vane pump was used as the backing pump for the gas line. All connections were 6 mm Swagelok with adapters for the capacitance manometer and water/nitrogen lines which were Swagelok VCR and 1/4" Swagelok connections respectively. H-series Nupro[®] valves were used to dose gases and isolate the gas line from the backing pump.

In the first version of the design, the gas line extended into the chamber and terminated in a straight Swagelok tube ending directly above the face of the powder sample. However, this resulted in the sample powder being blown from the crucible and settling on the chamber walls all the way to the gate valve (figure 4). The gate valve and the L-extension served in stopping any powder from reaching the turbopump, thus saving the pump from impaction and failure. This effect was understood to be due to the Swagelok extension acting as a jet, directing the dosed gas onto the sample. This was confirmed from observing the crucible and the large hole made in the sample powder as seen in figure 5. In order to overcome this effect in later designs, the Swagelok extension was bent at a 45 degree angle, facing away from the copper crucible, resulting in the water vapor not being dosed directly onto the powder sample. This is shown in figure 5.

The volume of the gas line is obtained from the ideal gas law (equation (1)) and assuming constant temperature. Table 1 lists the volumes of the different key parts of the rig—the gas line (V_L), the chamber (V_C) and the reference/water (V_R). Figure 6 identifies the different volumes involved in the experiment which have been marked with symbols for identification. The gas line volume is calculated first with a reference volume (sample cylinder used for water vapor dosing). The chamber volume is then calculated by keeping the gas line volume as the reference. Nitrogen was used to measure the volume due

to its inert and ideal gas properties in the (high) temperatures of interest

$$V_L = V_R \left(\frac{P_1}{P_{Eq}} - 1 \right). \quad (1)$$

There are four manual valves (as shown in figure 6) that are used to control the calibration and gas dosing procedures. They are listed in table 2 along with the specific connection details. During the experiments, the reference volume was replaced with a known volume of liquid distilled water which was used to dose a known pressure of steam into the gas line. The dosing procedures have been explained in section 4.

3. The sample

Cerium oxide (CeO_2) powder was chosen as a non-radioactive structural surrogate for SNF in this experiment. The use of CeO_2 allows for having copious amounts of sample/surface area, for such experiments, that is an idealized representation of the SNF surface but without the radioactivity that would make the chamber hazardous [18]. CeO_2 also exhibits similar lattice structure and parameters comparable to UO_2 and other actinide surfaces in SNF, making it an ideal surrogate for this study [19, 20]. However, cerium, like most lanthanides, exhibits only 3+ and 4+ oxidation states forming stable oxides— CeO_2 and Ce_2O_3 . This limits the applicability of cerium to chemically mimic the oxidation of actinides in SNF. Validation runs were conducted using CeO_2 as the apparatus was custom built for (SNF, actinide dioxide powders and sintered material) samples that exhibited low adsorption enthalpies [4], meaning it was expected that the sample would attain monolayers at low pressures and high temperatures. Moreover, the manometers, gas line setup, and powder sample quantity were all chosen based on the above assumptions.

The powder's particle size was selected based on the total amount of powder that was used and the amount of dosing water that was required to achieve a good sample coverage. This was also used to determine an optimum dose size and total number of dose steps until bulk saturation pressure. Thus, a size distribution of $<5 \mu\text{m}$ was obtained from Sigma Aldrich. The powder's surface area was experimentally determined to be equal to $18.516 \text{ m}^2 \text{ g}^{-1}$ with a relative error of 10% from a nitrogen isotherm at 77.35 K on a Quanta chrome NOVA 1200 surface area analyser. Additionally, the powder was also characterized using SEM and EDS analyses to ascertain the average particle size and probe for any impurities respectively (figure 7). The stoichiometry of the sample was not verified, as cerium is known to rapidly oxidize in air to form CeO_2 in the 4+ stable oxidation state of Ce. The bulk surfaces, however, are known to have oxygen defects and a presence of Ce(III) atoms, especially under vacuum conditions [21].

4. Experiment, results and discussions

All experiments were conducted at similar operating pressures (base vacuum, dosing steps and saturation pressures) and temperatures (the sample being placed at $100 \pm 5 \text{ }^\circ\text{C}$ and the

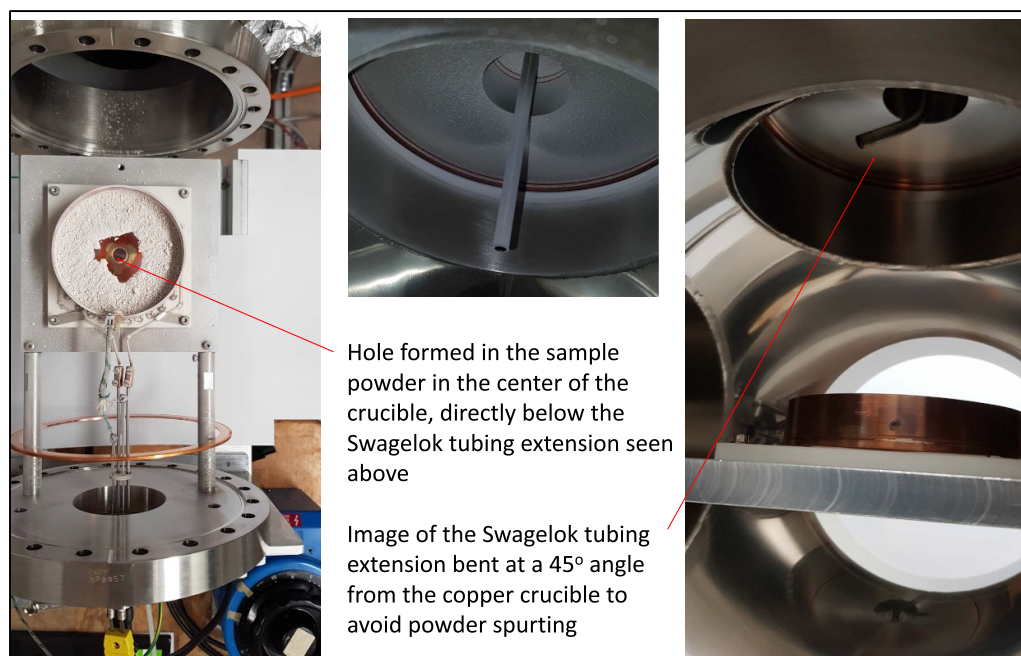


Figure 5. Images showing the aftereffects of the powder spurt and the modification in the apparatus adopted to mitigate it.

Table 1. Key volumes of important parts of the rig.

S. No.	Part	Volume (m ³)
1.	Gas line	$2.03 \times 10^{-05} \pm 2.00 \times 10^{-06}$
2.	Chamber	$1.70 \times 10^{-02} \pm 1.70 \times 10^{-03}$
3.	Reference	1.50×10^{-04} (Swagelok part)

chamber at 115 ± 5 °C). Experiment preparation involved pumping down the chamber, baking both the chamber and gas line, and maintaining the required thermal equilibrium using heating tapes controlled by separate Variacs (variable auto-transformers) for the chamber, sample holder and the gas line. The chamber pump-down procedure, before loading a sample, involved the following steps (referring to figure 3):

1. The gate valve and leak valve were ensured to be turned off before the pump-down process.
2. The backing pump on the chamber was allowed to run with the manual on/off valve 'off' until the Pirani gauge read a base vacuum of $\sim 10^{-2}$ mbar.
3. The gate valve was opened using the gate valve controller and the manual valve was gradually opened to the backing line low vacuum. At this point, the Pirani gauge reads the high pressures and slowly falls back to the 10^{-2} range (lower limit). The chamber pressure is noted on the IoniVac Combi gauge inside the chamber.
4. The turbopump was switched on when the pressures stabilized to a medium vacuum from the backing pump.

The pump-down procedure after loading the powder sample involved the following steps to prevent sudden bursts in pressure (referring to figure 3):

1. The gate valve and leak valve were ensured to be turned off before the pump-down process.
2. The backing pump on the chamber was allowed to run with the manual on/off valve turned 'off' until the Pirani gauge read a base vacuum of $\sim 10^{-2}$ mbar.
3. The manual on/off valve was opened, and the backing pump was allowed to pump down the volume bounded by the closed gate valve.
4. The gas line was pumped down similarly, ensuring the leak valve was fully closed.
5. The leak valve was gradually opened to pump down the main chamber through the gas line. This step was done in steps with initially having a constant leak rate of 80 mbar and reducing to 10 mbar as the chamber pressure decreased to low vacuum ranges (< 5 – 10 mbar).
6. As the gas line (and chamber) pressure reduced to ~ 1 – 5 mbar, the leak valve was closed, and the gate valve was opened to the backing pump pressure of $\sim 10^{-2}$ mbar.
7. The turbopump was switched on when the pressures stabilized to a medium vacuum from the backing pump.

The sample was dried before each experiment run at 200 ± 5 °C until the chamber pressure reached the base chamber pressure ($\sim 1.0 \times 10^{-6}$ mbar). The sample was held at this pressure until equilibrium was achieved for ~ 12 h before being cooled to experiment conditions (100 ± 5 °C). Separate heating tapes were used for the UHV chamber and the gas line and were controlled using Variacs. Heating tapes on the chamber extended down until the gate valve which is closed during the experiment and forms the chamber volume (figure 3). K-type thermocouples were used to measure the temperature on the heating tapes. Freeze, pump and thaw cycles were performed to degas the gas

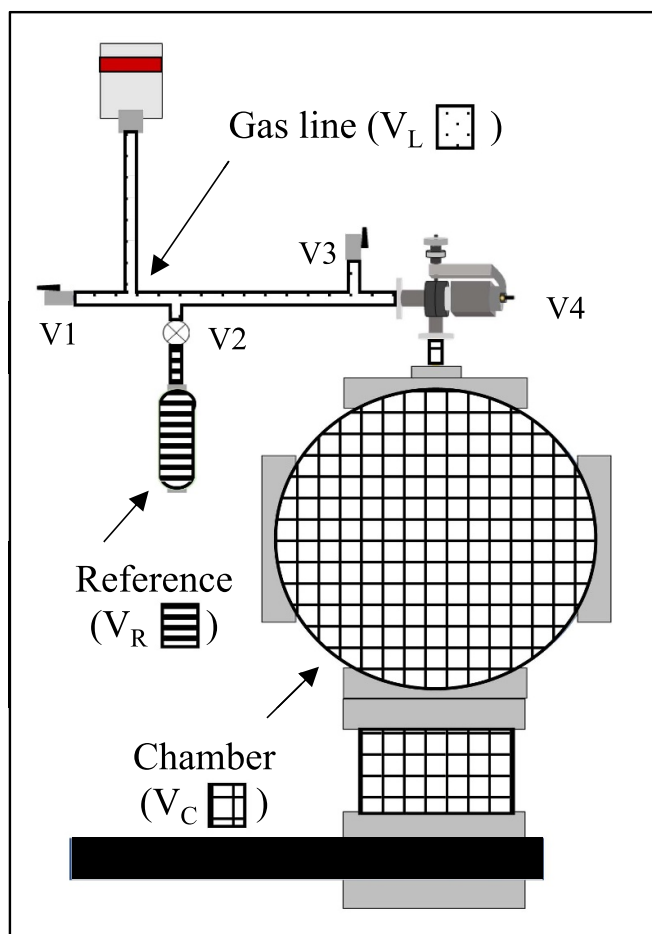


Figure 6. A schematic diagram showing the different volumes associated in the experimental test rig.

line before dosing [22]. The gas (steam) dosing procedure involved the following steps (referring to figure 6 and table 2):

1. Valve V1 was closed to isolate the gas line from the backing pump. The pressure in the gas line was noted.
2. The pressure in the gas line was increased by opening valves V2 or V3 based on the required gas (in the current setup shown in figure 6, V2 was for steam and V3 for nitrogen).
3. The valve (V2 or V3) was closed when the capacitance manometer reading showed the desired pressure. The pressure was allowed to stabilize until no change was observed and was noted down.
4. The leak valve (V4) was opened to dose the gas (steam) into the chamber, and it was held open until the pressure equilibrated. The equilibrium pressure reading in the capacitance manometer was noted down.
5. The leak valve (V4) was closed, and the gas line was pumped down by opening valve V1 to the backing pump.
6. Steps 1–5 were repeated for successive doses until the chamber pressure approached bulk saturation or a rapid rise in equilibrium pressure was noted.

Table 2. Valves used in the experiment rig and the corresponding connections.

S. No.	Valve	Connection
1.	V1 (On/off valve)	Backing pump
2.	V2 (Nupro valve)	Reference volume (V_R)
3.	V3 (On/off valve)	Nitrogen/Other gas line
4.	V4 (Leak valve)	Chamber

Results from two separate series of experiments, conducted on separate batches of $10.00 \text{ g} \pm 0.16 \text{ mg}$ CeO_2 (measured using an OHAUS PA114 mass balance), are discussed in this paper. The choice of 10 g was taken based on the powder particle size and surface area of the chamber, assuming loose packing of the powder and good gas access, in order to drive maximum adsorption onto the sample surface (as previously mentioned in section 2). An experiment series began with a fresh batch of (CeO_2) sample and consisted of multiple experiment runs wherein the sample was dosed with water vapour, and pressure readings were taken until bulk saturation was achieved. At the end of each run, the sample, the chamber, and the gas line were pumped down and baked as described above until a stable base vacuum was achieved. The base vacuum of the rig was observed to be improving after each experiment series and run (table 3). The term pristine powder is used in this study for the powder sample that was loaded into the apparatus for the start of an experiment series (i.e. for Run 1). Thus, Series 1—Run 1 and Series 2—Run 1 are experiments with a new batches of pristine powder. Series 1 consisted of a total of five Runs and Series 2 consisted of a total of seven Runs. Table 3 summarizes the conditions for the selected experiment runs discussed in this study.

Figures 8 and 9 show the equilibrium chamber pressure rise (after a particular dosing step) as a function of the dosed amount of water vapour (in mg) in selected experimental ‘runs’ from two separate ‘series’ of experiments, meaning with separate batches of CeO_2 . The cumulative dosed amount is simply an addition of the amount of water vapour in the gas line that was opened into the chamber at each step. Here, we assume that the entire amount of water vapor is directed into the chamber and onto the sample. The equilibrium chamber pressures after each dose account for what is adsorbed vs what is suspended in the gas phase (unabsorbed) inside the chamber. Thus, the trends seen in the equilibrium pressure variations as a function of the cumulative dose give an insight into the adsorption phenomenon observed in this study where—a higher equilibrium pressure for the same dosed amount of water vapour points to lower adsorption.

Figure 8 shows the increase in equilibrium chamber pressure achieved after each step dose vs the cumulative dose of water for the empty chamber (without the powder sample) and Runs 1 and 2 from Series 1 (table 3). In both the empty chamber runs, low dosing resulted in a high equilibrium pressure, meaning there was minimal sticking of the water vapour. The plot for pristine ceria (Series 1 Run 1) showed the highest

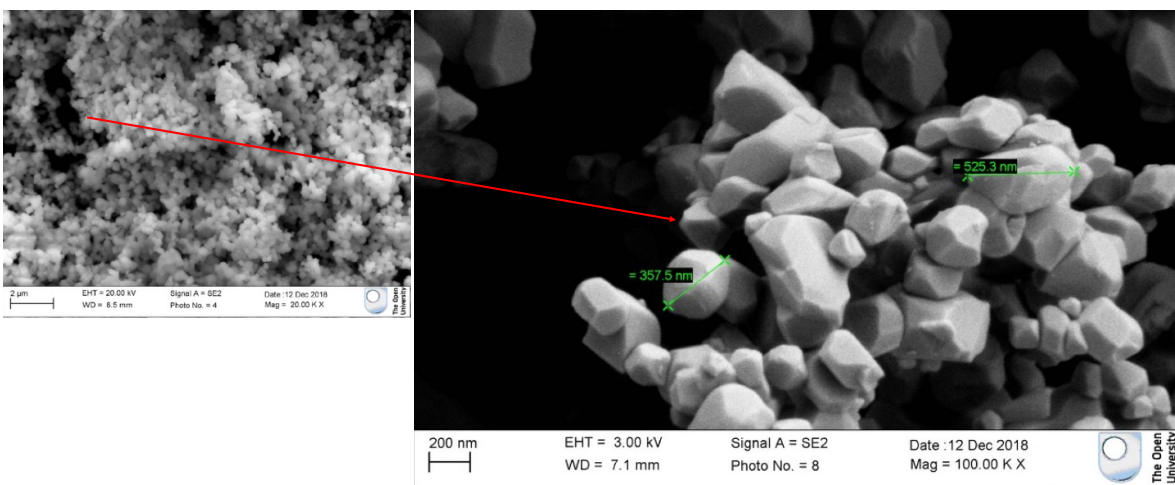


Figure 7. SEM images of the CeO₂ sample powder. The particles were seen to be agglomerated into clusters.

Table 3. Experiment details of selected runs discussed in the study.

Series number	Run number	Sample temperature (°C)	Starting vacuum (mbar)	Final pressure (mbar)
1	No sample Run 1	—	2.0×10^{-05}	34.18
	No sample Run 2	—	3.7×10^{-05}	42.32
	1 (pristine)	100 ± 5	1.3×10^{-06}	38.74
	2	100 ± 5	1.3×10^{-06}	46.60
2	No sample Run 1	—	1.0×10^{-06}	40.27
	No sample Run 2	—	1.0×10^{-06}	36.07
	1 (pristine)	100 ± 5	2.1×10^{-06}	32.58
	2	100 ± 5	6.8×10^{-07}	33.97

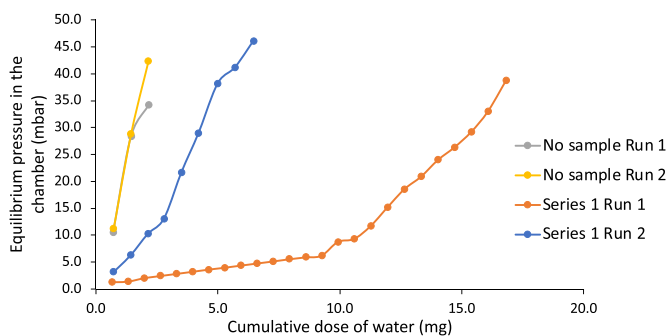


Figure 8. Cumulative dose of water vapour (mg) vs the equilibrium pressure (mbar) plots from experiment Batch—1. ‘No sample runs’ are control isotherms in an empty chamber.

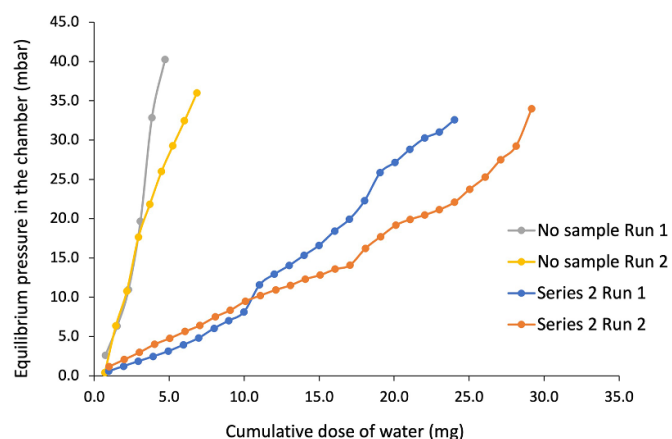


Figure 9. Cumulative dose of water vapour (mg) vs the equilibrium pressure (mbar) plots from experiment Batch—2. ‘No sample runs’ are control isotherms in an empty chamber.

adsorption among all runs in the series. Figure 9 shows the increase in equilibrium chamber pressure achieved after each step dose vs the cumulative dose of water for the empty chamber (without the powder sample), and in Runs 1 and 2 from Series 2 (table 3). As seen in figure 8, the empty chamber runs showed the least adsorption in Series 2, as the equilibrium pressure is seen to exponentially increase after small doses of water vapour. Runs 1 and 2 in Series 2 showed very similar trends with reproducible cumulative dose values for the same equilibrium pressures.

Although there were several failed adsorption runs in the two series which we attribute to leaks or cold spots, the general trend showed all the ceria runs to require higher water vapor dosage to achieve the equilibrium pressures obtained in empty chamber runs, meaning the ceria always adsorbed water at ~ 100 °C. As mentioned previously, the main difference between the two Series is the fact that the chamber was opened

between this period and that a new batch of sample was used. Differences in equilibrium pressure rise were naturally observed between runs of a specific Series despite following the same procedures for apparatus and sample preparation. However, the initial runs (with pristine ceria) always showed a trend of highest water vapour adsorption among all runs in the individual experiment Series (as seen in figures 8 and 9). This can be explained as a result of the physical and chemical changes in the sample (powder) surface from successive adsorption experiments. As discussed previously, water adsorption occurs in layers where the initial layers are assumed to be chemisorbed monolayers on the pristine powder, and there is a natural preference towards molecular adsorption as the surface adsorption sites are saturated. Chemically, ceria's affinity to lose oxygens from the surface and bulk [21] can be expected to increase the higher surface energies in the pristine powder (Run 1 of any batch) and increase the probability of strong dissociative chemisorption of water molecules. This is followed by a weaker physisorption and hydrogen bonding of subsequent water layers. We posit that perhaps the sample drying conditions adopted in the study only leads to the evaporation of the reversible physisorbed water leaving behind surface and bulk hydroxyls that require much higher temperatures to desorb, leading to reduced water vapor adsorption in the subsequent runs. This was also observed when the sample mass was measured as $10.0228 \text{ g} \pm 0.00245\%$ at the end of Series 1 pointing towards a total increase of $\sim 22.8 \text{ mg}$. This can be expected to be a result of the chemisorbed layers of water on the powder sample that did not evaporate at 200°C . The powder was also observed to have become crusty and hardened over the course of a series of experiment runs using a batch of powder sample, meaning there was some microstructural or chemical change. Such changes were also observed in PuO_2 by Stakebake and Steward [6]. The oxide sintering of the powder sample is expected to reduce the effective surface area available for adsorption and hence the number of sites that can be filled in subsequent runs is less. Thus, under the experiment conditions tested in this study, the pristine runs from the new sample are expected to show the full spectrum of chemisorption and physisorption in ceria and should therefore be used to calculate the total adsorbed water vapor in the samples. The subsequent runs showed a trend but are excluded beyond figure 9.

Figure 10 compares the equilibrium chamber pressures achieved per dose of water vapour (in mg) for experiment Run 1 from Series 1 and 2 (i.e. the pristine runs from two separate batches of $10.00 \text{ g} \pm 0.16 \text{ mg CeO}_2$ measured using an OHAUS PA114 mass balance) as a function of the cumulative dose. The experiments were started at similar base vacuums and taken up to similar final equilibrium pressures at the same sample and chamber temperatures (table 3). The graphs seem to overlap at low equilibrium pressures up to 11.50 mbar , after which the powder Ceria sample in Series 2 Run 1 seems to be adsorbing more water vapour as compared to the sample in Series 1 Run 1. The variation observed above $\approx 11.50 \text{ mbar}$ equilibrium pressure can be attributed to a chemical effect (such as oxide sintering) and successive modification of the

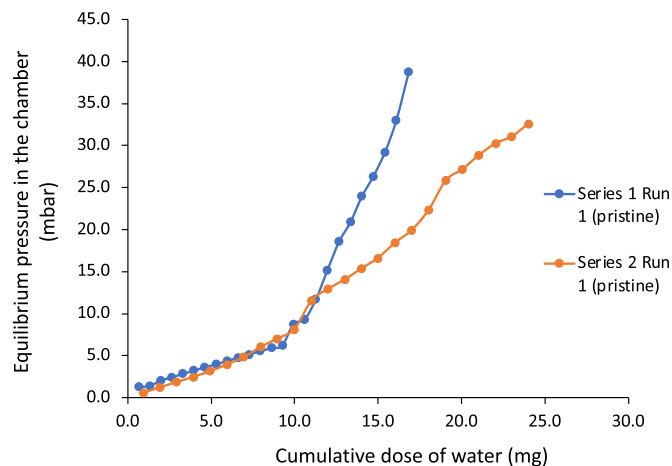


Figure 10. Cumulative dose of water vapour (mg) vs the equilibrium pressure (mbar) for pristine scans from experiment Batches—1 and 2.

powder surface as discussed above or be an issue with the apparatus driving a cold spot and resulting in local saturation of the water vapour in Series 2. Follow-up experiments, including post experiment sample surface analysis, are proposed to understand these discrepancies further.

The data presented in figure 10 was used to calculate and plot adsorption isotherms where the total amount of gas (steam) adsorbed was calculated based on the dosed amount and the pressure obtained in the chamber, i.e. amount of steam in gas phase as unadsorbed vapor. This is shown in figure 11 as a function of the relative equilibrium pressure

$$\frac{x}{m} = \frac{\text{Adsorbed amount} \times \text{molar mass of H}_2\text{O} \times 1000}{\text{mass of sample}} \left(\frac{\text{mg}}{\text{g}} \right)$$

$$\begin{aligned} \text{Adsorbed amount} &= \text{Cumulative steam dosed (mol)} \\ &\quad - \text{Amount of steam in gas phase (mol)}. \end{aligned}$$

Figure 11 also includes results from Stakebake and Steward looking at water adsorption on plutonium dioxide at 85°C [6]. The plutonium dioxide sample used in the study weighed 0.3181 g and was heat treated at 800°C in 300 torr of oxygen. In addition, the sample was outgassed at 900°C under vacuum for two hours prior to adsorption runs. The results were digitized using a MATLAB plot digitizer. The water adsorption trends from Stakebake and Steward's results show initial chemisorbed layers (Runs 1 and 2 [6]) where the adsorbed amount of water is posited to form a hydroxylated initial layer with the PuO_2 surface, and the second layer consists of hydrogen bonded water molecules; the subsequent water layers adsorbed over the initial chemisorbed layers (Runs 3–6 [6]) are seen to be weakly physisorbed and that process is completely reversible. It was seen that an evacuation of the sample after obtaining the reversible isotherm resulted in a constant amount of chemisorbed water being retained by the sample. A similar trend is assumed to be present in the results

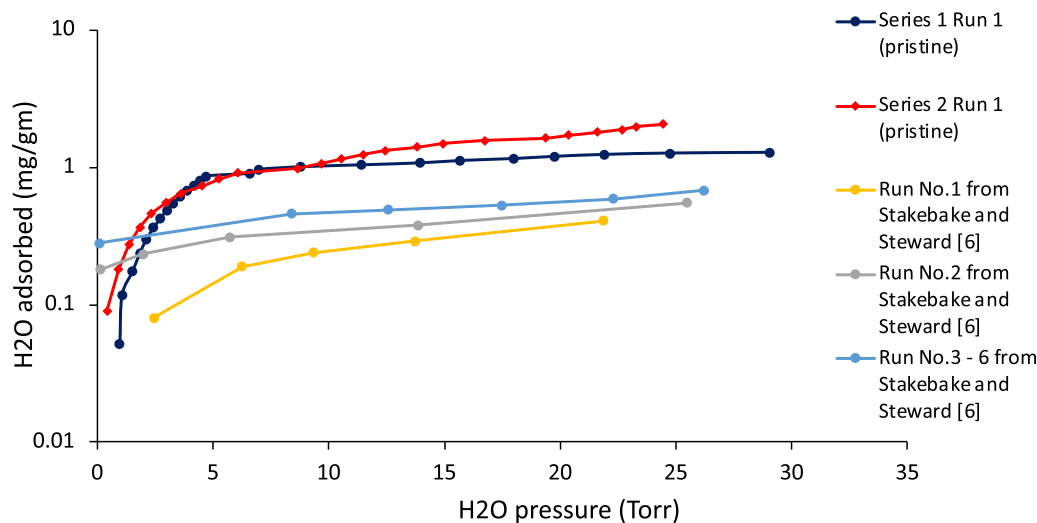


Figure 11. Plots showing the total amount of gas (steam) adsorbed as a function of equilibrium pressure in the chamber of pristine runs from experiment Batches—1 and 2.

obtained from this study, where the pristine fuel surface state was only present for the first run in a batch of experiments and not achieved in subsequent runs despite high temperature (~ 200 °C) vacuum drying following exposure to water vapor. This effect could mean that the accessible surface area of sample to the water vapor is highest during the first experiment run and reduces overtime, leading to inconsistencies in the experiment results.

Stakebake and Steward's study also observed adsorbed water and vacuum conditions causing 'oxide sintering' of the PuO_2 powder sample and a resulting $\sim 76\%$ reduction in accessible surface area. A similar effect was inferred in the ceria sample from this experiment where the texture of the powder had become crusty following multiple runs in batch of experiments.

The adsorption isotherms from the present study in figure 11 show a rapid increase in the amount of water condensed (adsorbed) on the sample until about 1 mg/gm of steam adsorption, after which it stabilizes to an equilibrium at higher equilibrium pressures. The increase in steam pressure to attain equilibrium between two batches in the study can be expected to be a result of variations in the sample chemistry, the chamber and gas line conditions and temperature fluctuations in the run. There is evidence to believe that a change in the local sample chemistry as a function of temperature and saturation pressure affects the rate of adsorption. There is the possibility of surface chemistries influencing the adsorption process (dissociative chemisorption), namely—the oxygen defects and the presence of stable Ce(III). Such defects are common in fluorite structures lattices and can be expected in SNF [18, 23].

Comparing the results with Stakebake and Steward's, the total amount of water vapor adsorbed on PuO_2 at 85 °C is less than what is adsorbed on CeO_2 , at 100 °C in the experiments reported here. The sample heat treatment between runs for Stakebake and Steward's study involved a 900 °C drying step as compared to the 200 °C drying in the present study. Although this is expected to result in a 'drier' sample and

a higher water adsorption, the effective sample surface area of PuO_2 used by Stakebake and Steward [6] is significantly lesser (2 m^2) than that of CeO_2 (185.16 m^2) used in this study. The amount adsorbed by CeO_2 at $100 (\pm 5)$ °C seems closer to what is seen at lower temperatures (27 °C and 50 °C) as reported by Stakebake and Dringman in other studies looking at PuO_2 —water adsorption [24]. Of course, the two substrates are different and hence equivalence should not be expected. The trends observed in PuO_2 postulated that the first adsorbed layer forms a hydroxylated layer while the second layer consists of hydrogen bonded water molecules. Thus, a dissociative chemisorption in the initial layers is followed by H-bonded physisorption. This theory has been consistent with CeO_2 —water adsorption as stated by Prin *et al* [25] and can be used to explain the differences in individual runs as discussed above.

5. Conclusions

This paper describes the construction and method development of an experimental apparatus to study the adsorption behaviours of steam on SNF (UO_2) surfaces at drying temperatures. Adsorption experiments were performed on CeO_2 , a structural surrogate for UO_2 . The preliminary results show that such surrogate fuel surfaces do attract and retain layers of water, even at hot and vacuum conditions. The results have been discussed and validated by comparison to literature studies of PuO_2 adsorption at similar temperatures. The main observations can be summarized as follows:

1. Ceria was seen to adsorb water vapour at 100 °C. Hence, it can be inferred that hot SNF can attract layers of water in the event of a cladding breach, and this points to the need for further experimental tests to understand the mode of adsorption, the surface energies involved and role of surface treatment in the adsorption phenomenon.

- Wetting and subsequent vacuum drying of ceria was observed to cause alterations in the surface texture and chemistry of the powder. Although no further characterization was conducted, other studies have observed a reduction in the surface area due to such changes.

This study highlights an experimental rig that was built to address a specific problem in the nuclear industry. The reader is cautioned that the results, although significant, are from preliminary work on the rig and has not been completely reproduced. The data obtained from the pilot studies have been compared to similar studies looking at water adsorption on SNF surfaces. The results suggest that there is a possibility for water carryover from hygroscopy in 'dried' (failed) fuels awaiting disposal. As regards to the handling of spent fuel, the initial results reported suggest that drying procedures are important. Specifically, attention is needed to limit the factors that can result in adsorption of water on fuel surfaces, for example, by employing more specific drying techniques for pinhole/failed breached fuel.

Future work should be aimed at conducting desorption experiment runs and further analysis through desorption spectroscopy to give complementary information such as the mass-to-charge ratio and abundance of gas-phase ions as a function of sample surface temperature. This will also help elucidate the chemisorption regime observed at lower partial pressures of steam adsorption by detecting H₂ and O₂ pressures.

Data availability statement

The data that support the findings of this study are openly available at the following URL/DOI: [10.21954/ou.ro.00013f99](https://doi.org/10.21954/ou.ro.00013f99) [26].

Acknowledgments

The authors would like to thank Dr Ross Springell and Dr Gavin Bell for their contributions to the development of the experimental apparatus. The authors would also like to thank the engineering and electrical workshops at the Open University, UK.

Funding

This work was funded by the Imperial Cambridge Open Centre for Doctoral Training with an Engineering and Physical Sciences Research Council (EPSRC) Grant EP/L015900/1.

ORCID iDs

Yadukrishnan Sasikumar  <https://orcid.org/0000-0003-1592-7979>

William J Nuttall  <https://orcid.org/0000-0002-6052-9657>

Nigel J Mason  <https://orcid.org/0000-0002-4468-8324>

References

- World Nuclear News 2021 Fuel failure confirmed at Taishan 1: regulation & safety—world nuclear news (available at: <https://world-nuclear-news.org/Articles/Fuel-damage-confirmed-at-Taishan-1>) (Accessed 18 October 2021)
- Johnson J A B 1977 Behavior of spent nuclear fuel in water pool storage U.S. Department of Energy Office of Scientific and Technical Information (<https://doi.org/10.2172/7284014>)
- Burns P C, Ewing R C and Navrotsky A 2012 Nuclear fuel in a reactor accident *Science* **335** 1184–8
- Alexandrov V, Shvareva T Y, Hayun S, Asta M and Navrotsky A 2011 Actinide dioxides in water: interactions at the interface *J. Phys. Chem. Lett.* **2** 3130–4
- Stultz J, Paffet M T and Joyce S A 2004 Thermal evolution of hydrogen following water adsorption on defective UO₂(100) *J. Phys. Chem. B.* **108** 2362–4
- Stakebake J L and Steward L M 1973 Water vapor adsorption on plutonium dioxide *J. Colloid Interface Sci.* **42** 328–33
- Murphy P M, Boxall C, Taylor R J and Woodhead D A 2013 Investigation of water adsorption on metal oxide surfaces under conditions representative of PuO₂ storage containers *ECS Trans.* **53** 81–94
- Haschke J M and Ricketts T E 1997 Adsorption of water on plutonium dioxide *J. Alloys Compd.* **252** 148–56
- Skomurski F N, Shuller L C, Ewing R C and Becker U 2008 Corrosion of UO₂ and ThO₂: a quantum-mechanical investigation *J. Nucl. Mater.* **375** 290–310
- Tegner B E, Molinari M, Kerridge A, Parker S C and Kaltsoyannis N 2017 Water adsorption on AnO₂ {111}, {110}, and {100} surfaces (An = U and Pu): a density functional theory + *U* study *J. Phys. Chem. C* **121** 1675–82
- LaVerne J A and Tandon L 2003 H₂ production in the radiolysis of water on UO₂ and other oxides *J. Phys. Chem. B* **107** 13623–8
- Montgomery R, Morris R N, Cantonwine P, Sasikumar Y and Keever T J 2024 Appendix C: rod internal pressure, void volume, and gas transmission tests *Sister Rod Destructive Examinations (FY21)*
- Jerden J L, Frey K and Ebert W 2015 A multiphase interfacial model for the dissolution of spent nuclear fuel *J. Nucl. Mater.* **462** 135–46
- Montgomery R, Sasikumar Y, Keever T, Skitt D, Bevard B and Nuttall W 2022 Appendix J: leaching of high burnup used nuclear fuel in De-ionized water *Sister Rod Destructive Examinations (FY21)*
- Owens C W 1978 Introduction to radiation chemistry, 2nd edition (Spinks, J. W. T.; Woods, R. J.) *J. Chem. Educ.* **55** A246
- Shoesmith D W 2000 Fuel corrosion processes under waste disposal conditions *J. Nucl. Mater.* **282** 1–31
- Springell R et al 2015 Water corrosion of spent nuclear fuel: radiolysis driven dissolution at the UO₂ /water interface *Faraday Discuss.* **180** 301–11
- Wang G, Batista E R and Yang P 2020 Water on actinide dioxide surfaces: a review of recent progress *Appl. Sci.* **10** 4655
- Aidhy D S, Wolf D and El-Azab A 2011 Comparison of point-defect clustering in irradiated CeO₂ and UO₂: a unified view from molecular dynamics simulations and experiments *Scr. Mater.* **65** 867–70
- Ye B, Oaks A, Kirk M, Yun D, Chen W-Y, Holtzman B and Stubbins J F 2013 Irradiation effects in UO₂ and CeO₂ *J. Nucl. Mater.* **441** 525–9

- [21] Mullins D R 2015 The surface chemistry of cerium oxide *Surf. Sci. Rep.* **70** 42–85
- [22] Luyckx G and Ceulemans J 1987 Deoxygenation, deaeration and degassing: a survey and evaluation of methods *Bull. Soc. Chim. Belg.* **96** 151–63
- [23] Spurgeon S R, Sassi M, Ophus C, Stubbs J E, Ilton E S and Buck E C 2019 Nanoscale oxygen defect gradients in UO_{2+x} surfaces *Proc. Natl Acad. Sci. USA* **116** 17181–6
- [24] Stakebake J L and Dringman M R 1968 Hygroscopicity of plutonium dioxide
- [25] Prin M, Pijolat M, Soustelle M and Touret O 1991 Characterization of a cerium dioxide powder from its equilibrium with water vapour *Thermochim. Acta* **186** 273–83
- [26] Sasikumar Y 2022 *Investigating the Solubility of Spent Nuclear Fuel*(The Open University) (<https://doi.org/10.21954/ou.ro.00013f99>)